nature nanotechnology

ARTICLES

https://doi.org/10.1038/s41565-018-0204-1

Corrected: Publisher Correction

# Controllable conductive readout in self-assembled, topologically confined ferroelectric domain walls

Ji Ma[1], Jing Ma[1], Qinghua Zhang[2], Renci Peng[1], Jing Wang[1,3], Chen Liu[1], Meng Wang[4], Ning Li[5], Mingfeng Chen[1], Xiaoxing Cheng[6], Peng Gao[5], Lin Gu[2], Long-Qing Chen[1,6], Pu Yu[4], Jinxing Zhang[3]* and Ce-Wen Nan[1]*

**Charged domain walls in ferroelectrics exhibit a quasi-two-dimensional conduction path coupled to the surrounding polarization. They have been proposed for use as non-volatile memory with non-destructive operation and ultralow energy consumption. Yet the evolution of domain walls during polarization switching makes it challenging to control their location and conductance precisely, a prerequisite for controlled read–write schemes and for integration in scalable memory devices. Here, we explore and reversibly switch the polarization of square $BiFeO_3$ nanoislands in a self-assembled array. Each island confines cross-shaped, charged domain walls in a centre-type domain. Electrostatic and geometric boundary conditions induce two stable domain configurations: centre-convergent and centre-divergent. We switch the polarization deterministically back and forth between these two states, which alters the domain wall conductance by three orders of magnitude, while the position of the domain wall remains static because of its confinement within the $BiFeO_3$ islands.**

Topological states with low-dimensional textures, such as vortices and domain walls (DWs), in ferroic materials are fundamentally important and technologically attractive in terms of thermodynamic stability at reduced dimensions, low threshold of controllability and exotic physical behaviours[1–5]. Apart from the numerous studies on magnetic DWs over the past century, ferroelectric DWs are attracting increased interest due to emerging functionalities, such as conduction, photovoltaic and magnetoelectric effects, and nanoscale integrated oxide electronic devices[6–10]. Very recently, several polar topologies (analogous to spin topologies) have been observed in low-dimensional confined structures, such as flux-closure quadrants in strained $PbTiO_3$ thin films[6] and polar vortices in $SrTiO_3/PbTiO_3$ superlattices[7,8]. The functionalities of these polar topologies and their deterministic control remain to be experimentally studied.

Local electrical conduction was discovered to occur in typical DWs (angles of 109°, 180° or 71° between the polarization directions in two adjacent domains) in multiferroic $BiFeO_3$ (BFO)[11,12], offering intriguing possibilities for nanometre-sized logic or data-storage applications. More importantly, the observed conductance at the DWs can be controlled by an electric field[13–17], providing a model system in which to achieve non-volatile control of charge transport with low energy consumption. In contrast to classical destructive readout devices in ferroelectric memories, prototype non-destructive readout memories based on ferroelectric DWs have recently been demonstrated[18,19], in which a parallel electrode geometry was designed so that conductive walls would be created during write/readout operations. However, such laterally controlled devices may reduce the memory density, and the restoration process shows an unstable nature of the charged DWs during switching[19]. Furthermore, without specific pinning, DWs in BFO might not appear at the same locations each time during polarization switching. For example, obvious changes in the stripe domain patterns in BFO films were observed during polarization switching, showing that the behaviour of the DW locations was not repeatable[20,21]. Conductive DWs with topological protection observed in hexagonal manganites show high stability but are challenging to control[22,23]. Thus, it is desirable to create controllable DW conduction with topological protection so that conduction with a vertical write/readout geometry (current perpendicular to the film plane) is accessible. Although substantial insight has been gained into the correlation between DW conduction and surrounding ferroelectric polarization, conduction at such DWs has been observed to exist only when assisted by electrical poling (scanning probe or parallel electrodes)[13,18,19,24,25] or in the form of natural defects[15,16,26,27], inhibiting their thermodynamic stability in a high-density array and affecting the deterministic writing and readout of each on/off state.

Here, we explore centre-type quad-domains with cross-shaped charged DWs in self-assembled square-shape BFO nanoislands. The geometrically determined vertex-like domain on each island is reversibly switchable between centre-convergent and centre-divergent states among four polar vectors under an electric field, where all polar vectors point to or away from the centre. We further demonstrate that the controllable conductance is enhanced by three orders of magnitude after electric-field switching of the centre-type domains. Such reversible conduction with persistent, repeatable and stable qualities in these self-assembled nanostructures is a step

[1]State Key Lab of New Ceramics and Fine Processing, School of Materials Science and Engineering, Tsinghua University, Beijing, China. [2]Beijing National Laboratory for Condensed Matter Physics, Institute of Physics, Chinese Academy of Science, Beijing, China. [3]Department of Physics, Beijing Normal University, Beijing, China. [4]State Key Laboratory of Low Dimensional Quantum Physics and Department of Physics, Tsinghua University, Beijing, China. [5]International Center for Quantum Materials and Electron Microscopy Laboratory, School of Physics, Peking University, Beijing, China. [6]Department of Materials Science and Engineering, Penn State University, University Park, PA, USA. *e-mail: jxzhang@bnu.edu.cn; cwnan@tsinghua.edu.cn

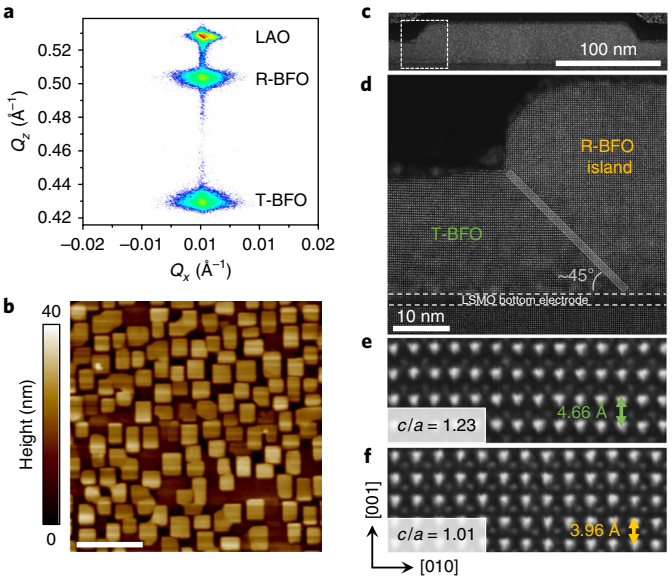


**Fig. 1 | Structural analysis of the $BiFeO_3$ nanoislands. a**, Reciprocal-space maps around the LAO (002) peak. $Q_x$ and $Q_z$ represent projected directions in the reciprocal space. **b**, Topography of BFO (001) thin film with self-assembled ordered nanoislands. Scale bar, 1 µm. **c**, Cross-sectional TEM image of a BFO island embedded in the film matrix. **d**, High-resolution TEM image from the island–matrix transition region marked by the dashed rectangle in **c**. The angle of the tilted bottom edge of the island (that is, the boundary between island and matrix) is approximately 45°. **e**,**f**, Atomically resolved HAADF STEM images of the BFO film matrix (**e**) and the BFO island (**f**). The lattice parameter and the lattice parameter ratio $c/a$ indicate the presence of the tetragonally distorted T-phase for the matrix and the rhombohedrally distorted R-phase for the island.

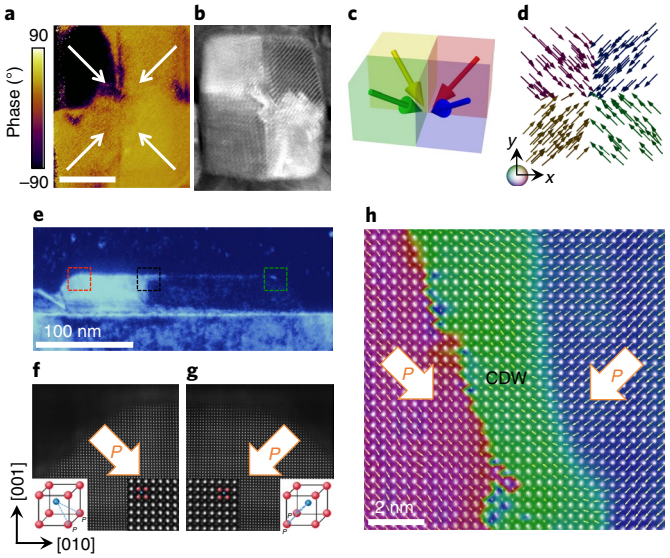


**Fig. 2 | Centre-convergent quad-domain structures of $BiFeO_3$ nanoislands. a**, In-plane PFM image, with the white arrows indicating the polarization directions (*P*). Scale bar, 100 nm. **b**, Plan-view low-angle annular dark-field image showing a square-shaped BFO nanoisland containing four sections with different polarization vectors. **c**, Schematic of the 3D polarization configuration of the centre-type domain structure in the BFO nanoisland. Arrows with different colours indicate different polarization vectors. **d**, Ferroelectric polarization vectors obtained by phase-field simulations, reproducing the centre-convergent quad-domains from a random initial state. **e**, Cross-sectional dark-field TEM image showing a vertical domain wall in a BFO island. **f**,**g**, Atomically resolved HAADF STEM images of the left (**f**) and right (**g**) edges of the island from the regions marked by the red and green dashed rectangles, respectively, in **e**, indicating that the polarization is directed inward to the island centre. The insets show schematic perspective views of the unit cell of BFO. Red symbols denote Bi atoms, and blue symbols represent Fe atoms. **h**, Atomically resolved HAADF STEM image of the H-H DW region highlighted by the black dashed rectangle in **e**. Vectors indicate the polarization directions across the charged domain wall (CDW) regions. Different polarization regions are marked by different colours.

towards non-destructive readout ferroelectric-based nanodevices with low energy consumption.

## Self-assembled nanoisland array

Epitaxial BFO thin films were grown on a 2-nm-thick (La,Sr)$MnO_3$ (LSMO) film on $LaAlO_3$ (LAO) (001) single-crystal substrates, where LSMO serves as bottom electrode (see Methods). Reciprocal-space mapping (Fig. 1a) and the $\theta$–$2\theta$ X-ray diffraction pattern (see Supplementary Fig. 1a) show that these BFO films contain a mixture of rhombohedrally distorted (R-phase) and tetragonally distorted (T-phase) perovskite structures. Unlike BFO thin films with a morphotropic phase boundary[28–31], in which T- and R-phases coexist in the form of a stripe feature without dislocations, our mixed-phase BFO thin films present a self-assembled, high-density array of square nanoislands, as shown in Fig. 1b. The low-magnification transmission electron microscopy (TEM) image in Fig. 1c indicates that the lateral size of the nanoislands is approximately 200 nm and that the BFO nanoislands (about 40 nm thick) are embedded in the BFO matrix (about 20 nm thick). To further reveal the structure of the islands, the BFO islands and matrix were characterized by high-angle annular dark-field scanning TEM (HAADF STEM). Figure 1d shows high-quality LAO/LSMO and LSMO/BFO interfaces and the boundaries between islands and matrix, in which the side edges of the islands are parallel to the [100] and [010] crystallographic orientations. The lattice parameters of these two regions were determined according to the magnified images shown in Fig. 1e,f. For the matrix, the out-of-plane and in-plane lattice parameters are 4.66 Å and 3.79 Å ($c/a \approx 1.23$), respectively, in agreement with those of the T-phase. For the islands, the out-of-plane and in-plane lattice parameters are 3.96 Å and 3.94 Å ($c/a \approx 1.01$), in agreement with those of the typical R-phase[28]. The R-phase BFO nanoislands grow from the bottom of the film, owing to partial strain relaxation, while the thin matrix surrounding the nanoislands forms as the T-phase, owing to the large in-plane compressive strain. According to previous work[32–34], the inhomogeneous strain state at the interface of the R-phase islands and T-phase matrix, combined with the competition between strain energy and surface energy of the system, contributes to the formation of the islands. In general, with increasing film thickness, BFO grown on LAO (001) substrates can show a distinct phase evolution from pure T-phase in a relatively thin (for example, <10 nm thick[31], completely strained) film to mixed R/T phases (10–300 nm thick[28,29]), and to a subsequent pure R-phase (>300 nm thick[29]) through relaxation of the epitaxial strain (see Supplementary Fig. 1b–d). In the present intermediate state, well-ordered R-phase islands are self-assembled in the T-phase matrix with a high density caused by appropriate strain and surface energies (Fig. 1b, Supplementary Fig. 1e). Such self-assembled ferroelectric nanoislands provide a favourable model system to study exotic domain structures.

## Switching of centre-type quad-domains

Piezoresponse force microscopy (PFM) and STEM revealed the ferroelectric domain structure of the BFO nanoislands. As shown in

Fig. 2a and Supplementary Fig. 2a, the in-plane projection of polarization in an individual island contains four vectors, each of which points inward towards the island centre, suggesting the formation of charged DWs between the adjacent domains. The out-of-plane polarization projection in the island is downward (Supplementary Fig. 2b). Further, the plan-view low-angle annular dark-field image (Fig. 2b) of the BFO nanoislands shows distinct diffraction contrast of four vectors that arises mainly from variation of the lattice orientation with different in-plane polarizations. The cross-sectional dark-field TEM image (Fig. 2e) from the reflection $\mathbf{g}=(0\bar{2}2)$ ($\mathbf{g}$ is diffraction vector) of the island presents two different domains divided by a vertical DW that grows from the bottom of the island. Furthermore, as shown in the high-resolution HAADF STEM images (Fig. 2f,g), the bright part on the left side and dark part on the right side have a polarization pointing along the body diagonal and towards the island centre, which is consistent with our PFM results. The STEM images also reveal a vertical 71° DW with head-to-head (H-H) polarization configration, as shown by vector mapping of atomic polar displacement in Fig. 2h. The vector mapping reveals that the charged DW has a width of about 3–5 nm, which is much thicker than the typical width of ~1 nm of the neutral-charged DWs[35]. This characteristic width probably arises because the polarization charges are distributed over a wide thickness of the walls, so that the depolarization field can be compensated to stabilize the charged DWs[35–37]. These experimental observations confirm that a centre-convergent quad-domain (vertex-like[3]) pattern with 71° charged H-H DWs is created in the BFO nanoislands, as schematically illustrated in Fig. 2c; this pattern differs from the previous model[14]. These cross-shaped charged DWs in the BFO nanoislands are formed by self-assembly over a large area rather than created either by scanning probe techniques or by ion etching/defect engineering[13,18,19,24,25].

For phenomenological understanding, phase-field modelling was performed to study the domain evolution from a random initial state according to the time-dependent Ginzburg–Landau equation (see Methods). Without an a priori assumption of the polarization distribution, as demonstrated in Supplementary Section B, the phase-field simulated polarization mappings (Fig. 2d and Supplementary Fig. 3) evolve towards a centre-convergent domain state in a BFO nanoisland, which is consistent with the experimental results. The formation mechanism for this domain pattern might be explained in the following manner. In the R-phase BFO islands, the ferroelectric polarization is aligned along the <111> directions of its pseudo-cubic structure. Furthermore, bottom edges tilted so that there is an angle of approximately 45° between the R-phase island and the matrix (Fig. 1d), combined with the constraint from the matrix, provide geometry and strain boundary conditions that energetically favour polarization parallel to the tilted bottom edges. Further, because the BFO films are n-type ferroelectric with electronic carriers (electrons liberated from oxygen vacancies)[2,12,16,26], the positive bound charges in the H-H DWs are more easily screened (and thus have lower energy) than the negative bound charges in the tail-to-tail (T-T) DWs[3], so the H-H DWs can be efficiently screened. Therefore, H-H but not the T-T DWs form spontaneously in the pristine nanoislands, as observed in our experiments. The phase-field simulations also demonstrate the formation of such a centre-convergent domain pattern with the H-H DWs screened by the compensating charges of $3.54\times10^{19}\,\mathrm{cm}^{-3}$. The concentration is roughly consistent with the estimate of about $10^{20}\,\mathrm{cm}^{-3}$ obtained from simple analytical phenomenological calculations[2,36,37] ($\sim P_N/(qt_{DW})$, where $P_N\approx40\,\mu\mathrm{C\,cm}^{-2}$ is the component of polarization normal to the DW, $t_{DW}\approx4$ nm the average DW width for the BFO islands and $q$ is the elementary electron charge). Such naturally emerging centre-type quad-domain patterns with cross-shaped charged DWs are rare in conventional ferroelectrics because of the additional electrostatic and/or strain energy cost[2]. Instead of being randomly pinned by extrinsic defects, the naturally emerging charged DWs in the BFO nanoislands are 'protected' by the formation of the fourfold vertices[3] and stabilized by the tilted bottom edge geometry and the constraints of cubic nanostructure. As a result, the self-assembled centre-convergent quad-domains are topologically protected and stabilized.

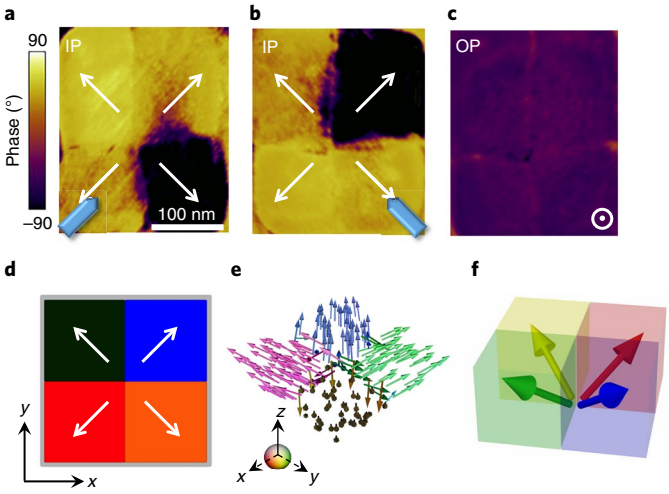


**Fig. 3 | Domain structure of $BiFeO_3$ nanoislands after polarization switching.** **a**,**b**, In-plane (IP) PFM image of the BFO island after switching (a) and in-plane PFM image with sample rotation by 90° relative to **a** (**b**), revealing a centre-divergent quad-domain configuration, where the white and blue arrows indicate the in-plane projections of the polarizations and a schematic of the cantilever, respectively. **c**, Out-of-plane (OP) PFM image of the BFO nanoisland after polarization switching, showing an upward polarization. **d**,**e**, Centre-divergent domain structure (**d**) and 3D image of polarization vectors of the centre-divergent domain (**e**), obtained from phase-field simulations. **f**, Schematic of the 3D polarization configuration of the centre-divergent domain structure in the BFO nanoisland.

The ferroelectric polarization of the BFO islands can be switched by the electric field. Interestingly, after the application of 3 V sample bias, the original H-H vectors transform into the T-T vectors that correspond to centre-divergent domains with cross-shaped charged DWs, as shown in Fig. 3a–c. Phase-field simulations (Fig. 3d,e, and Supplementary Fig. 4) were performed to understand the switching process. Similar to the stable initial state of the H-H DWs with a downward polarization, a stable upward polarization with the T-T DWs (Fig. 3d–f) forms in the BFO nanoislands after switching, in agreement with the PFM results (Fig. 3a–c). The difference between these two stable states is the type of accumulated compensating charge at the DWs; these charges are also responsible for the formation of the charged DWs. For the stabilization of spontaneously occurring H-H DWs, the density of the accumulated compensating charges is $3.54\times10^{19}\,\mathrm{cm}^{-3}$ (electrons) (Fig. 4d), whereas a screening charge density of $3.15\times10^{21}\,\mathrm{cm}^{-3}$ (holes) is necessary to stabilize the T-T DWs (see Supplementary Section C). When switched from the initial stable H-H domain pattern to the T-T domain pattern under an electric field, large numbers of holes delivered from the *p*-type LSMO electrode are injected into the film for compensation of the T-T charged walls. Both experimental results and simulations demonstrate that polarization in the BFO islands can be switched by means of a low electric field between two stable states with 71° charged DWs—that is, centre-convergent and centre-divergent quad-domains.

## Controllable large conductance of cross-shaped DWs

The self-assembled centre-type quad-domains of the BFO islands provide a model system in which to study local conduction in

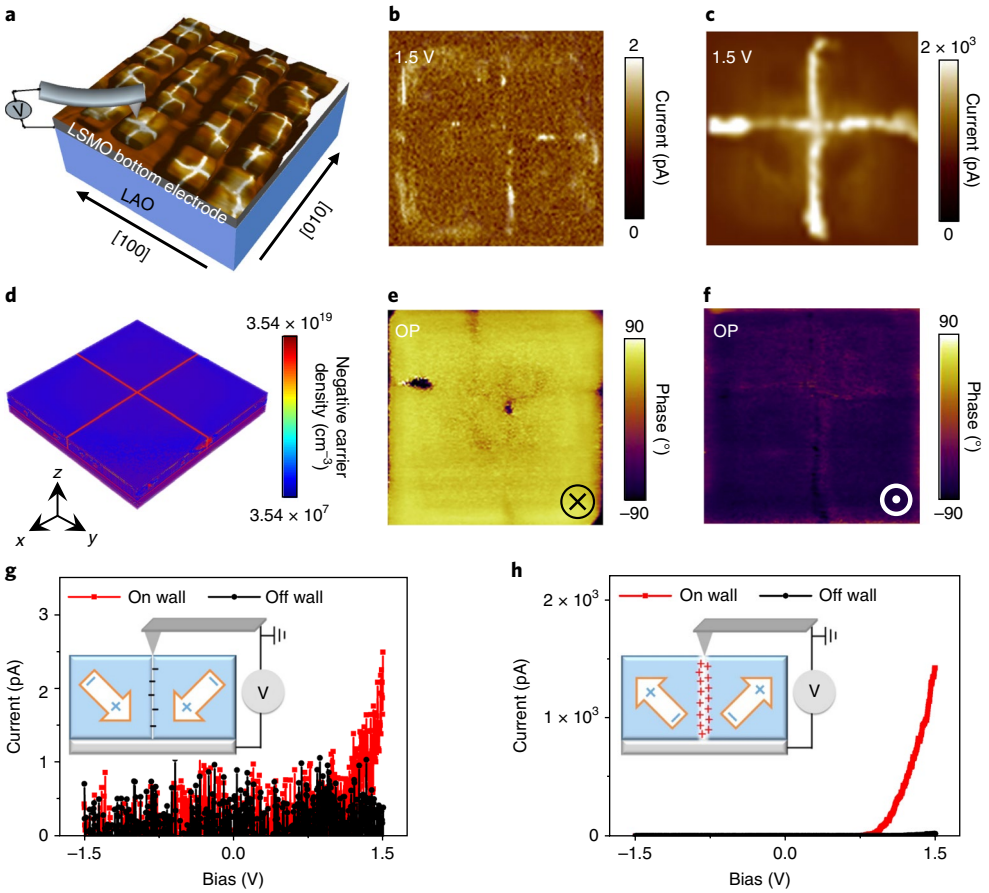


**Fig. 4 | Large conductance at charged domain walls in $BiFeO_3$ nanoislands. a**, Schematic of the experimental geometry for investigating conduction at the DWs of BFO nanoislands on LSMO on LAO: a movable grounded Pt/Ir-coated silicon tip acts as the top electrode. Through the application of an electrical field, the cross-shaped charged DWs are activated and show giant conductance on each island. **b**, Current map under 1.5 V bias at the initial state. **c**, Current map at the charged DWs under 1.5 V bias after polarization switching of the island. **d**, Phase-field simulations of the charge distribution on a BFO nanoisland with dimensions of 200 nm × 200 nm × 40 nm. The additional compensating negative charges were concentrated in the H-H DWs of the island. **e**, Out-of-plane PFM image of the BFO nanoisland in the initial state. **f**, Out-of-plane PFM image of the BFO nanoisland after 3 V switching. **g**, The corresponding *I*–*V* curve for the domain walls (on wall) exhibits picoampere-level current, and that for the domain (off wall) exhibits no current in the initial state **b**. **h**, Current–voltage curve showing nanoampere-level current corresponding to the switched state shown in **c**. Insets in **g** and **h** are schematics of the conduction in the initial and switched states.

charged DWs. As shown in Fig. 4a, strong current signals from the cross-shaped charged DWs across each island are observed through conductive atomic force microscopy (c-AFM) (see details in the Methods). At a voltage of 1.5 V, the measured current in the H-H charged DWs is several picoamperes (Fig. 4b,g), which is the same order of magnitude as that in traditional BFO DWs[11,12]. After polarization switching has occurred under an electric field to form the T-T charged DWs (Fig. 4e,f), the DWs show an enhancement (three orders of magnitude) of the conductance, with a current that can be as high as several nanoamperes (nA) at 1.5 V bias (Fig. 4c,h). This current is also increased by approximately three orders of magnitude relative to that for DWs in BFO thin films (see Supplementary Fig. 5) and is nearly an order of magnitude higher than that for charged DWs in La-doped BFO films[16]. Our observation of much higher conductance in T-T charged DWs with upward polarization (centre-divergent quad-domains) than in H-H charged DWs with downward polarization (centre-convergent quad-domains) is different from the cases of $BaTiO_3$ and $BiFeO_3$ thin films[24,25], where the conductance in H-H charged DWs created by scanning probe techniques was found to be orders of magnitude higher than that in T-T charged DWs. The charged DWs in the present BFO nanoislands are stabilized by the geometric-related boundary condition of the clamped BFO islands and the compensating charges that determine the conductance of the DWs. Because the charge carriers in the LSMO bottom electrode are p-type, the concentration of free electron carriers is low at the initial positively charged H-H DWs (inset to Fig. 4g), whereas a high concentration of free hole carriers provided by the LSMO electrode accumulates at the negatively charged T-T DWs after polarization switching (inset to Fig. 4h). Therefore, the conductance is low at the H-H charged DWs, whereas it is enhanced in the T-T configuration. Both H-H and T-T DWs show diode-type current–voltage (*I*–*V*) characteristics, which can be easily explained by a simple model based on the band diagrams (see Supplementary Section E). In the case of H-H DWs, a current flows for the forward bias, as the electrons can tunnel to the BFO conduction band from the Pt tip and then diffuse to the p-type LSMO bottom electrode (Supplementary Fig. 6b); however, vanishing current is observed for the backward bias, owing to scarce electrons injected into the BFO conduction band from p-type LSMO (Supplementary Fig. 6c). In the case of the T-T DWs, a much higher current flows for the forward bias because the holes can easily drift from the BFO valence band to the tip (Supplementary Fig. 6e); again, there is no obvious current for backward bias, owing to the scarcity of holes injected into the BFO valence band from the Pt tip (Supplementary Fig. 6f).

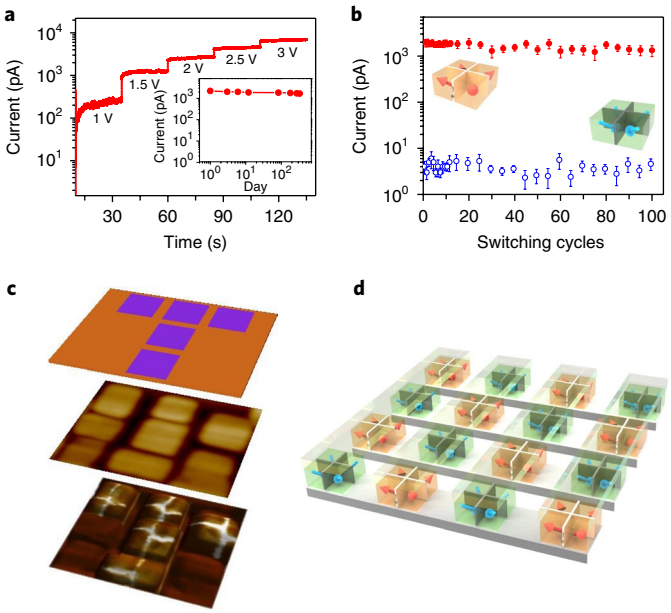


**Fig. 5 | Stability and repeatability of high conductance in charged DWs.** **a**, Time dependence of the current in the charged DWs under a sample bias of 1–3 V. Inset shows the time dependence of the current measured for a charged DW over 11 months. A stable current with a very slight decrease is visible. **b**, The repeatability of low and high conductance at the charged DWs measured across 100 cycles by repeatedly switching the island polarization between down and up states under −3 V and 3 V sample bias, respectively. The blue open circles and red filled circles are currents read at the polarization down and up states under 1.5 V, respectively. The insets are the corresponding schematics of two polarization configurations of the $BiFeO_3$ (BFO) nanoisland, which represent a high-conductance (on) state and low-conductance (off) state, respectively. **c**, Selectively writing a series of conductive BFO nanoisland arrays as a T pattern. **d**, Schematic of an envisaged cross-bar memory device using BFO nanoislands with charged DWs as storage bits.

The *I*–*V* measurements were repeated under various conditions (multiple scanning probe techniques; see Supplementary Fig. 7), from which we can confirm the high conductance in the cross-shaped DWs in the BFO islands. These experiments imply that the *I*–*V* characteristics should be different when using n-type bottom electrodes such as $SrRuO_3$.

## Stability and repeatability of domain-wall conduction

The measured current is persistent under different biases, as shown in Fig. 5a. Thus, the origin of this high conductance is not related to the DW disturbance[11]. Such a stable DW current also rules out field-induced migration of defects and oxygen vacancies[17]. Moreover, the measured current (see inset to Fig. 5a) remains fairly stable at the level of several nanoamperes over a period of several months. Figure 5b shows the repeatability of the low and high conductance for these two stable cross-shaped DWs under 1.5 V, measured by reversibly switching the polarization between the two states. The switching is fairly stable in 100 cycles between two conductive states with an on/off resistance ratio of $10^3$. Taking into consideration the controllable large area of ordered self-assembled BFO nanoislands, the DW-based devices have promise for applications. In Fig. 5c, we show the selective writing of a 'T' pattern in the array of BFO islands. Every selected nanoisland has a cross-shaped conduction path, which represents an 'on' state written by a positive electric field (3 V). Islands with the charged DWs in the low-conductance state represent the 'off' states. These on/off states are non-volatile, and the readout voltage can be as low as 1.5 V, which is non-destructive. A schematic cross-bar device structure with vertical write/readout geometry is shown in Fig. 5d. A much higher storage density could be achieved for this device by reducing the island size. Currently, the centre-type domain pattern with charged DWs is achieved in self-assembled BFO islands of size ~100 × 100 × 40 $nm^3$ (see Supplementary Fig. 8). The experimentally achievable lower limit for this size is currently unclear, because the growth conditions and related techniques could be varied for careful control of the interplay between the T- and R-phases and topological geometry at much smaller dimensions. However, phase-field simulations demonstrate that centre-type quad-domains with H-H DWs can be stable on BFO nanoislands with a lateral size as small as 16 nm when the thickness of the islands is reduced down to 10 nm (see Supplementary Section G and Supplementary Fig. 9). These results are expected to open avenues for further experimental and engineering explorations.

## Conclusions

Centre-type quad-domains accompanied by charged DWs naturally form in single BFO nanoislands, self-assembled in an array. Benefiting from topological protection of the quad-domains, we achieved reversible electric-field switching between the two stable centre-type domain states. The centre-convergent and centre-divergent quad-domains present spatially confined DWs, which show a conductance difference of three orders of magnitude. The polarization stability demonstrated over months and the switching stability for 100 cycles, together with the self-assembled growth, open routes towards mass manufacturing of DW-based devices with high stability and density.

## Methods

Methods, including statements of data availability and any associated accession codes and references, are available at https://doi.org/10.1038/s41565-018-0204-1.

Received: 13 February 2018; Accepted: 18 June 2018;
Published online: 23 July 2018

## References

1. Mermin, N. D. The topological theory of defects in ordered media. *Rev. Mod. Phys.* **51**, 591–648 (1979).
2. Seidel, J. (ed.) *Topological Structures in Ferroic Materials* (Springer, Cham, 2016).
3. Catalan, G., Seidel, J., Ramesh, R. & Scott, J. F. Domain wall nanoelectronics. *Rev. Mod. Phys.* **84**, 119–156 (2012).
4. Hang, F. T. & Cheong, S. W. Aperiodic topological order in the domain configurations of functional materials. *Nat. Rev. Mater.* **2**, 17004 (2017).
5. Vasudevan, R. K. et al. Domain wall conduction and polarization-mediated transport in ferroelectrics. *Adv. Funct. Mater.* **23**, 2592–2616 (2013).
6. Tang, Y. L. et al. Observation of a periodic array of flux-closure quadrants in strained ferroelectric $PbTiO_3$ films. *Science* **348**, 547–551 (2015).
7. Yadav, A. K. et al. Observation of polar vortices in oxide superlattices. *Nature* **530**, 198–201 (2016).
8. Damodaran, A. R. et al. Phase coexistence and electric-field control of toroidal order in oxide superlattices. *Nat. Mater.* **16**, 1003–1009 (2017).
9. Li, Z. et al. High-density array of ferroelectric nanodots with robust and reversibly switchable topological domain states. *Sci. Adv.* **3**, e1700919 (2017).
10. Kim, K. E. et al. Configurable topological textures in strain graded ferroelectric nanoplates. *Nat. Commun.* **9**, 403 (2018).
11. Seidel, J. et al. Conduction at domain walls in oxide multiferroics. *Nat. Mater.* **8**, 229–234 (2009).
12. Farokhipoor, S. et al. Conduction through 71° domain walls in $BiFeO_3$ thin films. *Phys. Rev. Lett.* **107**, 127601 (2011).
13. Balke, N. et al. Enhanced electric conductivity at ferroelectric vortex cores in $BiFeO_3$. *Nat. Phys.* **8**, 81–88 (2012).
14. Vasudevan, R. K. et al. Exploring topological defects in epitaxial $BiFeO_3$ thin films. *ACS Nano* **5**, 879–887 (2011).
15. Yang, C.-H. et al. Electric modulation of conduction in multiferroic Ca-doped $BiFeO_3$ films. *Nat. Mater.* **8**, 485–493 (2009).
16. Seidel, J. et al. Domain wall conductivity in La-doped $BiFeO_3$. *Phys. Rev. Lett.* **105**, 197603 (2010).

17. Maksymovych, P. et al. Dynamic conductivity of ferroelectric domain walls in $BiFeO_3$. *Nano Lett.* **11**, 1906–1912 (2011).
18. Sharma, P. et al. Nonvolatile ferroelectric domain wall memory. *Sci. Adv.* **3**, e1700512 (2017).
19. Jiang, J. et al. Temporary formation of highly conducting domain walls for non-destructive read-out of ferroelectric domain-wall resistance switching memories. *Nat. Mater.* **17**, 49–55 (2017).
20. Chu, Y.-H. et al. Nanoscale domain control in multiferroic $BiFeO_3$ thin films. *Adv. Mater.* **18**, 2307–2311 (2006).
21. Chen, D. et al. Interface engineering of domain structures in $BiFeO_3$ thin films. *Nano Lett.* **17**, 486–493 (2017).
22. Wu, W., Horibe, Y., Lee, N., Cheong, S.-W. & Guest, J. R. Conduction of topologically protected charged ferroelectric domain walls. *Phys. Rev. Lett.* **108**, 077203 (2012).
23. Meier, D. et al. Anisotropic conductance at improper ferroelectric domain walls. *Nat. Mater.* **11**, 284–288 (2012).
24. Sluka, T., Tagantsev, A. K., Bednyakov, P. & Setter, N. Free-electron gas at charged domain walls in insulating $BaTiO_3$. *Nat. Commun.* **4**, 1808 (2013).
25. Crassous, A., Sluka, T., Taganstev, A. K. & Setter, N. Polarization charge as a reconfigurable quasi-dopant in ferroelectric thin films. *Nat. Nanotech.* **10**, 614–618 (2015).
26. Li, L. et al. Giant resistive switching via control of ferroelectric charged domain walls. *Adv. Mater.* **28**, 6574–6580 (2016).
27. Rojac, T. et al. Domain-wall conduction in ferroelectric $BiFeO_3$ controlled by accumulation of charged defects. *Nat. Mater.* **17**, 322–328 (2017).
28. Zeches, R. J. et al. A strain-driven morphotropic phase boundary in $BiFeO_3$. *Science* **326**, 977–980 (2009).
29. Damodaran, A. R., Lee, S., Karthik, J., MacLaren, S. & Martin, L. W. Temperature and thickness evolution and epitaxial breakdown in highly strained $BiFeO_3$ thin films. *Phys. Rev. B* **85**, 024113 (2012).
30. Zhang, J. X., Zeches, R. J., He, Q., Chu, Y.-H. & Ramesh, R. Nanoscale phase boundaries: a new twist to novel functionalities. *Nanoscale* **4**, 6196–6204 (2012).
31. Pailloux, F. et al. Atomic structure and microstructures of supertetragonal multiferroic $BiFeO_3$ thin films. *Phys. Rev. B* **89**, 104106 (2014).
32. Tang, Y. L., Zhu, Y. L., Liu, Y., Wang, Y. J. & Ma, X. L. Giant linear strain gradient with extremely low elastic energy in a perovskite nanostructure array. *Nat. Commun.* **8**, 15994 (2017).
33. Macmanusdriscoll, J. L. et al. Strain control and spontaneous phase ordering in vertical nanocomposite heteroepitaxial thin films. *Nat. Mater.* **7**, 314–320 (2008).
34. Xue, F., Ji, Y. & Chen, L.-Q. Theory of strain phase separation and strain spinodal: applications to ferroelastic and ferroelectric systems. *Acta Mater.* **133**, 147–159 (2017).
35. Yudin, P. V., Gureev, M. Y., Sluka, T., Tagantsev, A. K. & Setter, N. Anomalously thick domain walls in ferroelectrics. *Phys. Rev. B* **91**, 060102 (2015).
36. Gureev, M. Y., Tagantsev, A. K. & Setter, N. Head-to-head and tail-to-tail 180° domain walls in an isolated ferroelectric. *Phys. Rev. B* **83**, 184104 (2011).
37. Bednyakov, P. S., Sluka, T., Tagantsev, A. K., Damjanovic, D. & Setter, N. Formation of charged ferroelectric domain walls with controlled periodicity. *Sci. Rep.* **5**, 15819 (2015).

## Acknowledgements

This work was supported by the Basic Science Center Program of NSFC (grant no. 51788104), NSFC (grant no. 51332001 and 51472140), the National Basic Research Program of China (grant no. 2016YFA0300103, 2016YFA0302300, and 2015CB921700) and the US DOE (grant no. DE-FG02-07ER46417). We thank H. Zhou for his discussion on band diagrams.

## Author contributions

C.-W.N., J.Z. and J.M. conceived the project and designed the experiments. J.M. grew the thin films and performed the electrical characterization. Q.Z. fabricated the TEM samples and performed the scanning TEM measurements with help from L.G. R.P. and X.C. performed the phase-field simulations under the supervision of L.-Q.C. and C.-W.N. N.L. carried out digital analysis of the STEM data under the supervision of P.G. M.W. performed the reciprocal-space mapping measurement under the supervision of P.Y. J.M., J.W., C.L., M.C. and P.Y. contributed to the PFM and c-AFM measurements and analysis. J.Z. and C.-W.N. wrote the manuscript, with input from all authors.

## Competing interests

The authors declare no competing interests.

## Additional information

**Supplementary information** is available for this paper at https://doi.org/10.1038/s41565-018-0204-1.

**Reprints and permissions information** is available at www.nature.com/reprints.

**Correspondence and requests for materials** should be addressed to J.Z. or C.-W.N.

**Publisher's note:** Springer Nature remains neutral with regard to jurisdictional claims in published maps and institutional affiliations.

## Methods

**Film growth.** The BFO thin films were grown on (001)-oriented LAO single-crystal substrates using the pulsed laser deposition method, with a 2-nm LSMO film grown as the bottom electrode. For deposition of both films, a KrF excimer laser, with a wavelength of 248 nm, repetition rate of 5 Hz and energy density of ~1.5 J cm$^{-2}$, was used. The films were grown at 700 °C under an oxygen pressure of 0.2 mbar. After deposition, the films were slowly cooled under an oxygen pressure of 200 mbar. The sample thickness was controlled by the growth time and then further confirmed by X-ray reflectometry measurement. The phase and crystallinity were confirmed by X-ray diffractometry.

**TEM images.** An ARM-200CF (JEOL) TEM was used for atomic structure analysis of the BFO thin films. Operated at 200 keV and equipped with double spherical aberration (Cs) correctors, the resolution limit of the probe defined by the objective pre-field is 78 pm. The collection angle for the HAADF image is 90–370 mrad. The TEM sample was prepared by using a focused ion beam. The cross-sectional lamella was thinned to 100 nm at an accelerating voltage of 30 kV with a maximum current of 2.5 nA. This was followed by fine polishing at 2 kV with 40 pA. The thickness of the sample is approximately 40 nm.

**PFM and c-AFM imaging.** AFM, PFM and c-AFM experiments were performed in ambient conditions at room temperature with an Infinity Asylum Research AFM. A Pt/Ir-coated tip on a Si cantilever (tip radius of 20 nm, force constant of 2.8 N m$^{-1}$ and a resonant frequency of 75 kHz) and other tips (Pt-, Ti/Ir- and doped-diamond-coated) were also used as movable top electrodes to apply bias voltages. To reconstruct the 3D domain structures, both the vertical and lateral PFM were conducted at different in-plane sample rotation angles. The piezo-cantilever scans along the $[\bar{1}10]$ direction of the BFO pseudo-cubic crystal, which is sensitive to the in-plane component of its ferroelectric polarization in the [110] and $[\bar{1}\bar{1}0]$ directions. Next, the sample is rotated by 90° with respect to the position of the cantilever so that the detailed in-plane polarization projection at an individual island can be determined. The bias voltage was applied to the tip (sample was grounded) and the sample (tip was grounded) for PFM and c-AFM measurements, respectively. For the PFM mode, the PFM signal was collected at the contact resonance frequency with an a.c. tip bias of 1 V. For c-AFM mode, the current was measured directly in the contact mode through a built-in current amplifier (0.5 pA to 20 nA).

**Phase-field simulations.** By using the phase-field approach[38], the spatial distribution $P_i(\mathbf{r})$ $(i=1,2,3)$ of the local polarization vector in the ferroelectric domain in an (001)-oriented BFO island can be obtained by solving the time-dependent Landau–Ginzburg equation[38]:

$$\frac{\partial P_i(\mathbf{r},t)}{\partial t} = -L\frac{\delta F_{\mathrm{p}}}{\delta P_i(\mathbf{r},t)} \tag{1}$$

where $L$ is a kinetic coefficient related to the domain-wall mobility and $F_{\mathrm{p}}$ is the total free energy of the BFO island with volume $V_{\mathrm{p}}$, expressed as

$$F_{\mathrm{p}} = \int_{V_{\mathrm{p}}}\int\int (f_{\mathrm{bulk}} + f_{\mathrm{elastic}} + f_{\mathrm{electric}} + f_{\mathrm{grad}})\,\mathrm{d}V \tag{2}$$

where $f_{\mathrm{bulk}}$, $f_{\mathrm{elastic}}$, $f_{\mathrm{electric}}$ and $f_{\mathrm{grad}}$ are the densities of the bulk free energy, elastic energy, electrostatic energy and gradient energy of the BFO, respectively. The expressions for $f_{\mathrm{elastic}}$, $f_{\mathrm{grad}}$ and $f_{\mathrm{electric}}$ of the BFO (001) islands can be found in the literature[39,40], and $f_{\mathrm{bulk}}$ is

$$f_{\mathrm{bulk}} = \alpha_1(P_1^2+P_2^2+P_3^2) + \alpha_{11}(P_1^4+P_2^4+P_3^4) + \alpha_{12}(P_1^2P_2^2+P_1^2P_3^2+P_2^2P_3^2) \tag{3}$$

where the Landau coefficients are listed as follows: $\alpha_1 = 4.9(T-1{,}103)\times10^5$ (C$^{-2}$ m$^2$ N), $\alpha_{11} = 6.5\times10^8$ (C$^{-4}$ m$^6$ N) and $\alpha_{12} = 1.0\times10^8$ (C$^{-4}$ m$^6$ N). The other materials parameters can be found in the literature[39]. The electrostatic energy density is obtained under a short-circuit boundary condition[41].

The discrete grid points of $220\Delta x\times220\Delta y\times42\Delta z$ with a real grid space of $\Delta x=\Delta y=1$ nm and $\Delta z=1.33$ nm are used to describe a three-phase system consisting of a BFO island, substrate and air layer. The dimensions of the simulated (001)-BFO island are 200 nm × 200 nm × 40 nm with a tilt angle of 45° towards the inside (with the appearance of a reversed trapezoid) from its half height, as shown in Supplementary Fig. 3a–c. The width of domain walls was assumed to be 2 nm in the phase-field simulations. The compensated charges are artificially introduced at the domain walls. The formation of the initial stable H-H domains was simulated from a random state under a bias voltage of −0.5 V on the bottom electrode.

**Data availability.** The data that support the plots within this paper and other findings of this study are available from the corresponding author upon reasonable request.

## References


38. Wang, J. et al. Effect of strain on voltage-controlled magnetism in $BiFeO_3$-based heterostructures. *Sci. Rep.* **4**, 4553 (2014).
39. Zhang, J. et al. Three-dimensional phase-field simulation of domain structures in ferroelectric islands. *Appl. Phys. Lett.* **92**, 122906 (2008).
40. Zhang, J. et al. Effect of substrate-induced strains on the spontaneous polarization of epitaxial $BiFeO_3$ thin films. *J. Appl. Phys.* **101**, 114105 (2007).
41. Li, L., Hu, S. Y., Liu, Z. K. & Chen, L.-Q. Effect of electrical boundary conditions on ferroelectric domain structures in thin films. *Appl. Phys. Lett.* **81**, 427–429 (2002).